Atmospheric Research 235 (2020) 104799

Contents lists available at ScienceDirect

Atmospheric Research

journal homepage: www.elsevier.com/locate/atmosres

Classifying aerosol particles through the combination of optical and physical-chemical properties: Results from a wintertime campaign in Rome (Italy)

S. Valentini[a], F. Barnaba[b], V. Bernardoni[a], G. Calzolai[c], F. Costabile[b], L. Di Liberto[b], A.C. Forello[a], G.P. Gobbi[b], M. Gualtieri[d], F. Lucarelli[c,e], S. Nava[c,e], E. Petralia[d], G. Valli[a], A. Wiedensohler[f], R. Vecchi[a,*]

[a] Department of Physics, Università degli Studi di Milano and INFN-Milan, 20133 Milan, Italy
[b] CNR Institute of Atmospheric Sciences and Climate, Via Fosso del Cavaliere 100, 00133 Rome, Italy
[c] INFN-Florence, 50019 Sesto Fiorentino, Italy
[d] ENEA – SSPT – MET – Atmospheric Pollution Laboratory (INAT), via Martiri di Monte Sole 4, 40129 Bologna, Italy
[e] Department of Physics and Astronomy, Università degli Studi di Firenze, 50121 Florence, Italy
[f] Leibniz Institute for Tropospheric Research, Permoserstrasse 15, 04318 Leipzig, Germany

ARTICLE INFO

Keywords:
Intensive optical properties
High time resolution
Aerosol classification schemes

ABSTRACT

The "Carbonaceous Aerosol in Rome and Environs" (CARE) experiment took place at a Mediterranean urban background site in Rome (Italy) deploying a variety of instrumentation to assess aerosol physical-chemical and optical properties with high-time resolution (from 1 min to 2 h). In this study, aerosol optical properties, chemical composition, and size distribution data were examined with a focus on the analysis of several intensive optical properties obtained from multi-wavelength measurements of aerosol scattering and absorption coefficients. The spectral behaviour of several quantities related to both aerosol composition and size was explored, analysing their high-time resolved temporal patterns and combining them in order to extract the maximum information from all the available data.

A methodology to separate aerosol types using optical data only is here proposed and applied to an urban area characterised by a complex mixture of particles. A key is given to correctly disentangle cases that could not be distinguished observing only one or few parameters, but that can be clearly separated using a suitable ensemble of optical properties.

The SSCAAE, i.e. the wavelength dependence of the Single Scattering co-albedo 1-SSA (where SSA is the Single Scattering Albedo) - that efficiently responds to both aerosol size and chemical composition – resulted to be the best optical intensive parameter to look at for the discrimination between episodes characterised by specific aerosol types (e.g. sea salt, Saharan dust) and more mixed conditions dominated by local emissions. However, this study also highlighted that it is necessary to combine temporal patterns of different optical parameters to robustly associate SSCAAE features to specific aerosol types. In addition, the complete chemical speciation and the high-time resolved size distribution were used to confirm the aerosol types identified via a combination of aerosol optical properties. Look-up tables with most suitable ranges of values for optical variables were produced; therefore, these pieces of information can be used at the same site or at locations with similar features to quickly identify the occurrence of aerosol episodes. Graphical frameworks (both from the literature and newly designed) are also proposed; for each scheme features, advantages, and limitations are discussed.

1. Introduction

Atmospheric aerosol is a complex mixture of suspended particles characterised by a huge variability in terms of chemical composition, size and shape. Aerosols can have a direct (by direct scattering and absorption) and indirect (by impacting on cloud formation and albedo) effect on atmospheric radiation (IPCC, 2013). Moreover, atmospheric aerosol is known to have detrimental effects on human health (Dockery

* Corresponding author at: Department of Physics, Università degli Studi di Milano and INFN-Milan, 20133 Milan, Italy.
E-mail address: roberta.vecchi@unimi.it (R. Vecchi).

https://doi.org/10.1016/j.atmosres.2019.104799
Received 7 August 2019; Received in revised form 8 November 2019; Accepted 29 November 2019
Available online 30 November 2019
0169-8095/

et al., 1993; Pope et al., 2002).

Estimates of the climate impacts of atmospheric aerosol and their optical properties are affected by very large uncertainties; nevertheless, direct measurements of aerosol optical properties are not usually performed by air quality (AQ) monitoring networks, in contrast to particle concentration and chemical composition, often performed for different size fractions. Aerosol optical properties are related to the size and composition of the particles, as well as to their mixing state (e.g. Bond and Bergstrom, 2006). Spectral scattering and absorption properties depend on the considered aerosol type; therefore, simultaneous measurements of multi-wavelength aerosol optical properties, chemical composition, and size distribution can improve our knowledge about atmospheric particles impact on the radiative forcing and air quality.

Several classification schemes have been proposed in the literature to distinguish aerosol types and mixtures. Most of these methods make use of column-integrated properties usually retrieved from remote-sensing data, such as those provided by the global network of ground-based sun and sky radiometers AERONET (Aerosol Robotic Network) or obtained by Sun photometers (e.g. Dubovik et al., 2002; Gobbi et al., 2007; Kalapureddy et al., 2009; Russell et al., 2010; Giles et al., 2011, 2012; Cazorla et al., 2013; Rupakheti et al., 2019). There are also few studies dealing with in-situ measurements of optical properties, both ground-based and airborne (e.g. Yang et al., 2009; Lee et al., 2012; Costabile et al., 2013; Cappa et al., 2016; Donateo et al., 2018; Romano et al., 2019). As pointed out by Schmeisser et al. (2017), the majority of the existing classification schemes work well at sites where the aerosol characteristics are fairly homogeneous, while their performance is worse in areas that experience a heterogeneity of particle sources and/or episodes characterised by aerosol transported from e.g. deserts or oceans. The methods proposed to distinguish PM types are sometimes supported by chemical composition, size distribution data, or back trajectory analyses; however, these pieces of information are not usually included in the classifying approaches themselves.

Data analysed in this paper were collected in the frame of the CARE Experiment (Carbonaceous Aerosol in Rome and Environs), which was carried out in Rome (Italy) using a variety of instruments and techniques to obtain a comprehensive and highly time-resolved picture of the aerosol properties at a Mediterranean urban background site. Indeed, several studies in recent literature (e.g. Timonen et al., 2010; Lucarelli et al., 2015; Costabile et al., 2017) pointed out the importance of shorter time scale (< 1 h) to study atmospheric processes and source variability. The CARE campaign was carried out at a site impacted by different local emission sources and sometimes affected by medium-long range transport of e.g. sea salt or Saharan dust. An overview of measurements performed and methodologies applied during the CARE experiment is given by Costabile et al. (2017).

A phenomenology of specific episodes characterised by aerosol with different properties is given exploiting all the available information about high-time resolved optical properties, chemical composition, and size distribution of atmospheric aerosol. The main objective here is to find out one or more possible combinations of intensive optical parameters that can be used as a tool to identify aerosols with different origin. In addition, graphical classification schemes reported in the literature were applied and some were newly developed to visually distinguish specific episodes and aerosol types via 2D plots of optical parameters. These representations appear useful to have a first hint on the typologies of particles observed during a campaign, even though they are not able to clearly disentangle different contributions, especially when atmospheric aerosol is dominated by mixtures of particles emitted by a variety of sources. In these cases, it is shown here that, exploiting multi-wavelength optical properties measured with high-time resolution, only the combined analysis of their temporal patterns allows to identify the dominant contributions.

2. Material and methods

2.1. Site description

The CARE experiment took place from January 27th to February 28th 2017 at an urban background site in downtown Rome. Due to its geographical position (in the middle of the Mediterranean Sea) and its meteorological conditions, this site can experience the advection of air masses transported from the Sahara Desert (Barnaba and Gobbi, 2004; Gobbi et al., 2007; Barnaba et al., 2017; Gobbi et al., 2019) or from the sea (Perrino et al., 2009). The CARE measurement site is also affected by local urban sources such as vehicular traffic and biomass burning for heating and cooking (Costabile et al., 2017, 2019).

2.2. Aerosol characterisation techniques

A detailed list of the instruments deployed during the CARE experiment and their operating conditions has been already reported in Costabile et al. (2017). Instruments and techniques which produced data here analysed will be shortly described in the following. Where not specified, instruments were operated at ambient relative humidity (RH).

2.2.1. Wavelength-dependent optical properties

On-line instruments continuously measured multi-wavelength PM10 scattering and absorption coefficients with a time resolution of 1 min. In this study, 5-minute averages of each parameter are considered in order to reduce data noise.

A 3-wavelength integrating Nephelometer (Aurora 3000, Ecotech) measured dry aerosol scattering coefficient $\sigma_s(\lambda)$ at 450, 525, and 635 nm. Total scattering coefficients were corrected for truncation error according to Müller et al. (2011a).

On-line dry aerosol absorption coefficient $\sigma_a(\lambda)$ at 7 wavelengths (370, 470, 520, 590, 660, 880, and 950 nm) was retrieved by equivalent Black Carbon (eBC) concentrations measured by a dual-spot Aethalometer (AE33, Magee Scientific) (Drinovec et al., 2015) and using instrument-specific Mass Absorption Cross sections (MAC) at different wavelengths.

Moreover, a Multi-Angle Absorption Photometer (MAAP, Thermo Scientific) was used to measure eBC concentration at RH $< 30\%$. From these data, $\sigma_a(637)$ was retrieved using the MAC of 6.6 m^2/g set in the MAAP and a wavelength correction factor of 1.05 as reported in Müller et al. (2011b).

2.2.2. Chemical analyses

Both on-line and off-line techniques were used to assess aerosol chemical composition (elements, carbonaceous fractions, non-refractory components) on different size fractions with time resolution from 30 min to 2 h.

PM2.5 samples collected with 1-hour time resolution using a streaker sampler were analysed off-line as for elemental composition by Particle Induced X-Ray Emission (PIXE) analysis (Calzolai et al., 2015). This technique allows the detection and quantification of $Z > 10$ elements.

A Sunset Field Thermal-Optical Analyzer (Model-4 Semi-Continuous OC-EC Field Analyzer – Sunset Laboratory inc.) measured elemental carbon (EC) and organic carbon (OC) in PM2.5 with a 2-hour time resolution.

An Aerodyne Aerosol Chemical Speciation Monitor (ACSM; Ng et al., 2011) provided PM1 non-refractory chemical components (organic matter, sulphate, ammonium, nitrate, and chloride ions) on-line. The instrument operated at RH $< 30\%$ with 30-minute time resolution and 1-hour averages were then calculated. Organic aerosol (OA) concentration apportioned among the sources by the SoFi software (Canonaco et al., 2013) was also analysed as an additional information; vehicular traffic (HOA), oxygenated secondary aerosol (OOA), and

biomass burning (BBOA) were the major components taken into account.

2.2.3. Particle number size distributions

To obtain particle number size distribution (PNSD), a Scanning Mobility Particle Sizer (TROPOS-SMPS) and an Aerodynamic Particle Sizer (APS, TSI) were employed during the CARE campaign. Both instruments were operated with a time resolution of 5 min. SMPS and APS covered the 8–700 nm range in electrical mobility diameter (d_m) and 0.5–20 μm in aerodynamic diameter (d_a), respectively. To obtain a unique number size distribution in the range 8 nm ≤ d_m ≤ 10 μm, APS data were converted to a d_m-based size distribution (i.e. dN/dlog(d_m)) and then merged to SMPS output following the procedure described in Khlystov et al. (2004). More details about the PNSD calculation at the CARE site can be found in Costabile et al. (2017) and in Alas et al. (2019).

3. Calculations

3.1. Aethalometer data corrections

The multi-wavelength aerosol absorption coefficient $\sigma_a(\lambda)$ was obtained by an AE33 Aethalometer, which gives eBC concentration using instrument-specific MAC values at seven wavelengths (e.g. 10.35 m^2/g at 660 nm). As described in Drinovec et al. (2015), the instrument internal software retrieves $\sigma_a(\lambda)$ from attenuation measurements and corrects them for loading (k parameter) and multiple scattering (C factor) effects. It is noteworthy that literature studies (e.g. Collaud Coen et al., 2010; Segura et al., 2014) pointed out the site-specificity and possible wavelength dependence of these effects.

As evidenced by some recent literature studies (e.g. Goetz et al., 2018), the C factor equal to 1.57 currently fixed in AE33 to convert attenuation into absorption can lead to a significant overestimation of the $\sigma_a(\lambda)$ by this instrument. Aiming at reducing this bias, in this work the availability of parallel (independent) optical measurements was exploited and - following Collaud Coen et al. (2010) –the loading-corrected C factor (here C_{corr}) was inferred via a linear regression analysis between the attenuation coefficient (loading-corrected) $\sigma_{atn,k}(660)$ calculated from the eBC concentration given by the AE33 and $\sigma_a(637)$ measured by the MAAP. Indeed, the MAAP is often considered as the reference instrument for filter-based measurements of aerosol light absorption coefficient (Müller et al., 2011b), and no simultaneous in-situ σ_a data were available for the CARE campaign. However, Hyvärinen et al. (2013) showed that when eBC concentration is high, the MAAP response lacks in linearity; in this study a non-linear behaviour at $\sigma_a(637) > 100$ Mm^{-1} was observed, thus only MAAP data giving $\sigma_a(637) < 100$ Mm^{-1} were considered in the regression $\sigma_{atn,k}(660)$ vs $\sigma_a(637)$.

The AE33 attenuation coefficient $\sigma_{atn,k}(660)$ was retrieved as follows:

$$\sigma_{atn,k}(660) = \sigma_a(660)\cdot C = [eBC(660)]\cdot MAC_{AE33}(660)\cdot C = [eBC(660)]\cdot 10.35\cdot 1.57.$$

The linear fit (performed with a Deming regression – see Fig. S1) had intercept compatible with zero (within 95% confidence interval) and a slope (i.e. the C_{corr}) of 2.66 that was used to correct the AE33 absorption coefficients at all wavelengths, following the approach developed by Collaud Coen et al. (2010) and neglecting the possible wavelength-dependence as controversial results are reported in the literature so far.

The corrected $\sigma_a(\lambda)$ from AE33 data were then calculated as:

$$\sigma_{a,corr}(\lambda) = \sigma_a(\lambda)\cdot C/C_{corr} = \sigma_a(\lambda)\cdot 1.57/2.66.$$

For the sake of simplicity, $\sigma_{a,corr}(\lambda)$ calculated with this procedure will be referred to as $\sigma_a(\lambda)$ in the following.

3.2. Intensive optical parameters

Wavelength dependences of scattering and absorption coefficients, represented respectively by Scattering Ångström Exponent (SAE) and Absorption Ångström Exponent (AAE), have been used in literature (e.g. Cazorla et al., 2013; Cappa et al., 2016) to distinguish different aerosol types. Indeed, while SAE is mainly related to particle size, AAE is more linked to aerosol composition, even though it is influenced by particle size distribution as well. Consequently, the combination of these two parameters (SAE and AAE) can provide information about the origin and properties of the studied aerosol.

In order to highlight possible stronger or weaker dependences of optical properties in some spectral regions, SAE and AAE were here calculated at different wavelength pairs. SAE(λ_1,λ_2) and AAE(λ_1,λ_2) were thus obtained as

$$SAE(\lambda_1,\lambda_2) = -\frac{\ln(\sigma_s(\lambda_1)/\sigma_s(\lambda_2))}{\ln(\lambda_1/\lambda_2)}$$

$$AAE(\lambda_1,\lambda_2) = -\frac{\ln(\sigma_a(\lambda_1)/\sigma_a(\lambda_2))}{\ln(\lambda_1/\lambda_2)}$$

where $\lambda_1 < \lambda_2$.

With a similar equation Extinction Ångström Exponent EAE(λ_1,λ_2) was also inferred from extinction coefficients $\sigma_e(\lambda)$ calculated at Nephelometer wavelengths (i.e. 450, 525, and 635 nm) as $\sigma_e(\lambda) = \sigma_a(\lambda) + \sigma_s(\lambda)$.

Due to the difference in the operating wavelengths of instrumentation used for measurements of scattering and absorption properties, $\sigma_a(\lambda)$ was reported to 450, 525, and 635 nm (i.e. the three operating λs of the Nephelometer). Since the absorption coefficient wavelength dependence can be represented by a power law ($\sigma_a(\lambda)\sim\lambda^{-AAE}$) with good approximation, the quantity AAE(fit) was calculated via a power-law fit of all 7-λ $\sigma_a(\lambda)$ to exploit all the available absorption spectral range.

For each of the three operating λs of the Nephelometer, the resulting $\sigma_a(\lambda)$ was then obtained as $\sigma_a(\lambda) = \sigma_a(\lambda_{ref})\left(\frac{\lambda}{\lambda_{ref}}\right)^{-AAE(fit)}$ where λ_{ref} is the nearest wavelength at which absorption data were available (i.e. 470, 520, and 660 nm for the AE33).

To better analyse the spectral behaviour of $\sigma_a(\lambda)$, the variation in AAE calculated employing different wavelength pairs was considered as the AAE itself may vary with the wavelength (Eck et al., 1999; Schuster et al., 2006; Moosmüller and Chackabarty, 2011). Indeed, even though the absorption wavelength dependence is usually represented by a simple power law, it has to be noted that especially when different aerosol components (e.g. Black Carbon, Brown Carbon and mineral dust) contribute to light absorption, the spectral behaviour can be more complicated; this feature is commonly referred to as spectral curvature.

The parameter used to quantify this effect will be hereafter referred to as dAAE(λ_1,λ_2,λ_3); it represents the spectral curvature of $\sigma_a(\lambda)$, computed as the derivative of AAE as a function of ln(λ). This calculation is similar to the one performed to obtain the curvature of Aerosol Optical Depth (AOD) often used by the AERONET network as a proxy for particle size (Kaufman, 1993; Eck et al., 1999; Schuster et al., 2006). Therefore, dAAE(λ_1,λ_2,λ_3) was calculated as:

$$dAAE(\lambda_1,\lambda_2,\lambda_3) = 2\cdot\frac{AAE(\lambda_1\lambda_2) - AAE(\lambda_2\lambda_3)}{\ln(\lambda_3/\lambda_1)}$$

where $\lambda_1 < \lambda_2 < \lambda_3$.

It is noteworthy that several dAAE were calculated using different λ combinations. Finally, dAAE(450,635,880) was selected as it responded well to absorption spectral variations. The 450–880 nm range was preferred to 370–950 nm interval in order to limit the possible bias reported by Zotter et al. (2017) at the shortest wavelength of 370 nm and because λ = 880 nm is the reference λ used by the Aethalometer to retrieve eBC concentration. In addition, AAE calculated using also 370 nm did not show a response to specific aerosol types as significant

as the one obtained when using 450 nm.

Aerosol absorption coefficients corrected for multiple scattering and adjusted for different wavelengths were also used to calculate the Single Scattering Albedo (SSA), representing the fraction of light extinction that is scattered. In the present work, SSA was retrieved at 450, 525, and 635 nm as $SSA(\lambda) = \sigma_s(\lambda)/\sigma_e(\lambda)$.

As pointed out by some authors (e.g. Moosmüller and Chackabarty, 2011; Costabile et al., 2013; Ealo et al., 2016; Titos et al., 2017) also the SSA wavelength dependence might be useful to give hints of variations in aerosol size and composition, as it responds to both physical and chemical properties. Specifically, $dSSA/d\lambda$ can serve as an indicator of the aerosol type especially at sites where Saharan dust transport events are detected (Collaud Coen et al., 2004; Yang et al., 2009; Costabile et al., 2013; Romano et al., 2019). For instance, Valenzuela et al. (2015) exploited spectral SSA to distinguish between so-called dust or non-dust periods, i.e. periods influenced or not by advections of aerosol from the Sahara desert.

Single Scattering Albedo Ångström Exponent (SSAAE) was also computed following Moosmüller and Chackabarty (2011):

$$SSAAE(\lambda_1,\lambda_2) = SAE(\lambda_1,\lambda_2) - EAE(\lambda_1,\lambda_2)$$

Indeed, as $\sigma_s(\lambda) \approx s\cdot\lambda^{-SAE}$ and $\sigma_e(\lambda) \approx e\cdot\lambda^{-EAE}$ (where s and e are constants), it follows:

$$SSA(\lambda) = \frac{\sigma_s(\lambda)}{\sigma_e(\lambda)} \approx \frac{s}{e}\cdot\frac{\lambda^{-SAE}}{\lambda^{-EAE}} = \frac{s}{e}\cdot\lambda^{-(SAE-EAE)} = \frac{s}{e}\cdot\lambda^{-SSAAE}$$

Since extinction is usually dominated by scattering, SSAAE is likely the difference between two quantities (SAE and EAE) with comparable values. For this reason, in most cases SSA is expected to have a weak wavelength dependence and high uncertainties; therefore, it was not taken into account here. Opposite, the single scattering co-albedo $SSCA = 1\text{-}SSA = \sigma_a(\lambda)/\sigma_e(\lambda)$ has a wavelength dependence which can be represented by the Single Scattering Co-Albedo Ångström Exponent (SSCAAE) (Moosmüller and Chackabarty, 2011), here computed as

$$SSCAAE(\lambda_1,\lambda_2) = AAE(\lambda_1,\lambda_2) - EAE(\lambda_1,\lambda_2)$$

It is noteworthy that co-albedo wavelength dependence does not depend on the relative contribution of absorption to extinction but only on the difference in their wavelength dependence. Moreover, being EAE comparable with SAE in most cases, SSCAAE is sensitive to both particle size (via EAE) and composition (through AAE), thus it is itself a combination of intensive optical properties describing different aerosol characteristics.

SSAAE shows the same features too but the range of variability of its absolute values is small compared to SSCAAE for typical atmospheric conditions (i.e. $SSA > 0.5$); thus, in this work SSCAAE was preferred as more effective in discriminating aerosol with different characteristics detected during specific episodes (see Section 4.1).

For all optical parameters calculated with two wavelengths, the widest Nepehlometer λ range (450–635 nm) was used to avoid extrapolation of $\sigma_s(\lambda)$ from 635 nm to 880 nm. Indeed, calculations performed with other couples of wavelengths (450–525 and 525–635) did not show significantly different features; the upper limit at 880 nm was considered for dAAE calculation only.

For the sake of clarity, Table 1 reports a synthesis of the optical parameters used in this work and their definitions.

3.3. Optical source apportionment

To further confirm the identification of aerosol types (see Section 4.1.2), the well-known Aethalometer model (for detail see e.g. Sandradewi et al., 2008) was applied to estimate the fossil fuel (FF) and biomass burning (BB) contributions to the measured absorption coefficient. Indeed, the availability of multi-wavelength absorption coefficients by the AE33 allowed the apportionment of such contributions using $AAE(FF) = 0.9$ and $AAE(BB) = 1.68$, as suggested by Zotter et al. (2017) when site-specific values are lacking.

4. Results and discussion

In the following, a detailed analysis of temporal patterns for intensive optical properties taken into account for aerosol classification is reported.

4.1. Temporal patterns of aerosol intensive optical properties – episodes and aerosol types identification

Temporal patterns of 1-h averaged SSCAAE(450,635), SAE(450,635), AAE(450,635), dAAE(450,525,635), and dAAE(450,635,880) are shown in Fig. 1. High time-resolution temporal behaviour for multi-wavelength scattering, absorption coefficients, and SSA, together with concentration of chemical components and particle number in different size ranges can be found in the Supplementary Material.

As discussed in Section 3, SSCAAE is sensitive to both particle size and composition, thus very high or low values are likely indicative of aerosol with particular properties. During the CARE experiment, SSCAAE had a median value of 0.2 and the 5th and 95th quantiles equal to −0.1 and 1.2, respectively. Interestingly, in some periods SSCAAE values appeared significantly higher than the median value for the campaign; three events with SSCAAE(450,635) values larger than 1 occurred on 3–6 February (hereafter referred to as first episode), 24–25 February (hereafter referred to as second episode), and for a few hours in the afternoon of February 26th (hereafter referred to as third episode).

Temporal patterns of SAE, AAE, and dAAE calculated with two λ triads (exploring different wavelength ranges) were analysed to look for different responses of these intensive properties among the three events during which SSCAAE was almost the same.

Comparing several intensive optical properties (Fig. 1), it was evident that the three episodes identified via SSCAAE temporal pattern represented events with different characteristics. In particular, SAE had significant lower values during the first two events and AAE was low in the period 3–6 February, higher during the second episode, and reached its absolute maximum in correspondence to the last one. The absorption spectral curvature dAAE(450,635,880) resembled the AAE(450,635) pattern, whereas dAAE(450,525,635) was not sensitive to the event occurring between February 24th and 25th.

In the next sections, episodes detected looking at intensive optical

Table 1
Intensive optical parameters used in this work.

Parameter name	Definition	Symbol
Single Scattering Albedo	$\sigma_s(\lambda)/\sigma_e(\lambda)$	$SSA(\lambda)$
Single Scattering co-albedo	$\sigma_a(\lambda)/\sigma_e(\lambda) = 1\text{-}SSA(\lambda)$	$SSCA(\lambda)$
Scattering Ångström Exponent	$-\ln[\sigma_s(\lambda_1)/\sigma_s(\lambda_2)]/\ln(\lambda_1/\lambda_2)$	$SAE(\lambda_1,\lambda_2)$
Absorption Ångström Exponent	$-\ln[\sigma_a(\lambda_1)/\sigma_a(\lambda_2)]/\ln(\lambda_1/\lambda_2)$	$AAE(\lambda_1,\lambda_2)$
Extinction Ångström Exponent	$-\ln[\sigma_e(\lambda_1)/\sigma_e(\lambda_2)]/\ln(\lambda_1/\lambda_2)$	$EAE(\lambda_1,\lambda_2)$
Absorption spectral curvature	$2[AAE(\lambda_1,\lambda_2)\text{-}AAE(\lambda_2,\lambda_3)]/\ln(\lambda_3/\lambda_1)$	$dAAE(\lambda_1,\lambda_2,\lambda_3)$
Single Scattering co-albedo Ångström Exponent	$AAE(\lambda_1,\lambda_2)\text{-}EAE(\lambda_1,\lambda_2)$	$SSCAAE(\lambda_1,\lambda_2)$

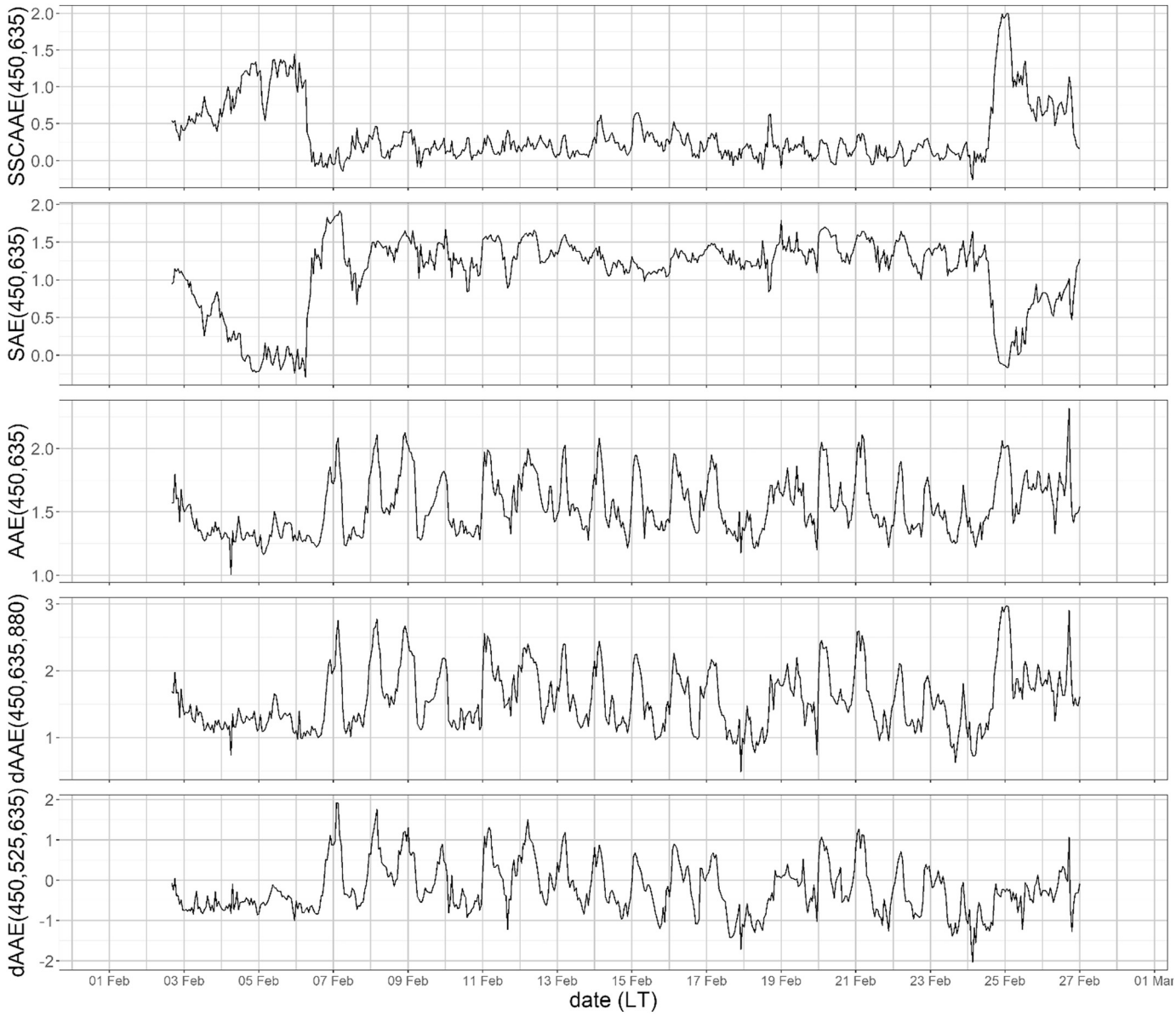

Fig. 1. Temporal patterns of SSCAAE(450,635), SAE(450,635), AAE(450,635), dAAE(450,635,880), and dAAE(450,525,635) during the CARE campaign.

parameters will be analysed in detail in order to distinguish the aerosol origin and physical-chemical characteristics responsible for the observed features in optical properties. In particular, periods characterised by advection-dominated and local sources-dominated aerosols will be addressed with the aim of checking the effectiveness of SSCAAE as the key parameter to quickly identify the presence of specific aerosol events.

4.1.1. Advection-dominated aerosol types

As already mentioned, the first episode was characterised by high SSCAAE values especially between February 3rd and 6th. As shown in Fig. 1, SAE(450,635) was low (below 0.5), indicating the predominance of large particles. Moreover, SSA(λ) was quite high (above 0.8) and exhibited a negative wavelength dependence (Fig. S4) thus further suggesting a significant contribution of particles with large diameters, as also reported by Takemura et al. (2002) for desert dust and sea salt (with a weaker wavelength dependence). During this period $\sigma_a(\lambda)$ was low (see Fig. S3) and AAE(450,635) was small (about 1.3), thus suggesting that the absorption spectral behaviour was dominated by Black Carbon (BC) contribution from local fresh traffic emissions, typically associated to AAE = 1, as also shown by Costabile et al. (2019). Finally, both dAAE(450,525,635) and dAAE(450,635,880) were lower than the campaign average, confirming a weak wavelength dependence of the absorption coefficient.

All these data together were suggestive of a sea salt advection episode; indeed, sea salt aerosol is generally characterised by quite large particles (from 0.5 to tens of micrometres – Ramachandran, 2018) and it does not typically contribute to $\sigma_a(\lambda)$ wavelength dependence due its negligible absorption coefficient. The attribution to a desert dust event (that can show similar SAE values) was excluded as higher AAE values are typically observed for this aerosol type (as explained in the following).

The sea salt transport episode identified through optical parameters was confirmed by particle number in different size ranges and chemical composition data.

Total particle number in the ranges 1 μm $< d_a <$ 2.5 μm and 2.5 μm $< d_a <$ 10 μm - that will be referred to as intermodal and coarse fractions, respectively - was calculated. From February 3rd to February 6th a large increase in number concentration of the intermodal and coarse fractions was observed in agreement with the

indication given by SSA wavelength dependence and consistently with results shown by Costabile et al. (2019).

During the sea salt episode, particle number concentrations in the intermodal and coarse size fractions were higher and sub-micrometric/intermodal ratio was lower (both of one order of magnitude) than in the rest of the campaign. It is noteworthy that during the period 3–6 February three sub-events were identified due to significant differences in aerosol properties. Indeed, the ratio of intermodal/coarse fractions was similar to previous days until the late afternoon of February 3rd (even though concentration of super-micrometric aerosol is already high), it subsequently peaked in the evening of February 4th and increased again in late morning in February 5th. It is noteworthy that these sub-events can also be detected by a more detailed analysis of SSCAAE, exhibiting a first small peak contemporary to the period of stable intermodal/coarse ratio on February 3rd, and two periods with values higher than 1 interrupted by a minimum corresponding to low SSA values and an increasing number concentration of sub-micrometric particles compared to the one in intermodal and coarse size fractions (Fig. S8).

A focus on chemical composition can be seen in Fig. 2, that represents temporal patterns of Na, Mg, Cl, V, Ni and S concentrations measured by PIXE analysis on PM2.5 streaker samples.

The sea salt advection episode (see Fig. 2) was characterised by a simultaneous increase in Na, Cl, and Mg concentrations - reaching 1158, 2518, and 362 ng/m^3, respectively - compared to average values of 92, 38, and 33 ng/m^3 detected during the rest of the campaign. Sea salt aerosol fresh emissions are typically identified through diagnostic ratios for bulk sea water (Seinfeld and Pandis, 1998), e.g. Cl/Na (1.8) and Mg/Na (0.12). It has to be noted that sea salt Cl in aerosol particles can be depleted due to heterogeneous reactions with other compounds occurring in the atmosphere (Seinfeld and Pandis, 1998), whereas Mg and Na are not involved in these processes; as a consequence, the Cl-to-Na ratio measured in sea salt aerosol can be lower than the one calculated based on bulk sea water composition, while Mg-to-Na ratio is maintained. As Na and Mg can be originated by multiple sources (e.g. sea salt, crustal material, industrial processes), when using the above mentioned diagnostic ratio only the contribution to the concentration of these elements due to sea salt should be taken into account. In this work, the elemental concentration was assessed by PIXE, therefore the concentration of sea salt Na (ssNa) was calculated following Diapouli et al. (2017). During the first episode, the ssNa-to-Na ratio was on average 0.95 ± 0.04, therefore the total Na concentration was used to calculate diagnostic ratios, to avoid further uncertainties related to assumptions in the ssNa calculation. In the first sub-event (February 3rd) Mg-to-Na ratio (0.16 ± 0.08) was fairly in agreement with the expected value of 0.12 while Cl-to-Na ratio was much lower (0.06 ± 0.02) than the one expected for fresh sea salt. The diagnostic ratios were thus suggesting that aged sea salt particles impacted on the sampling site and that Cl was likely depleted by atmospheric reprocessing during the plume transport (Seinfeld and Pandis, 1998). Indeed, on February 3rd (afternoon) peaks in V, Ni, and S concentrations - well known tracers for ship emissions (Viana et al., 2009) - were also registered. These chemical fingerprints confirmed that this first sub-event corresponded to the impact of a plume of aged and polluted marine aerosol.

An increase in SSCAAE and peaks in Cl, Na, and Mg concentrations characterised the second sub-event (February 4th). The Cl/Na and Mg/Na ratios were 1.79 ± 0.75 and 0.14 ± 0.01, respectively, i.e. comparable to diagnostic ratios for fresh sea salt. In this episode no significant contribution from anthropogenic components (e.g. V, Ni, EC) was observed, thus indicating the advection of clean marine air mass to the sampling site.

On February 5th, a third SSCAAE peak was registered and the aerosol characteristics were similar to the previous period but for smaller Cl/Na ratio (0.88 ± 0.38) and concentrations of S, V, and Ni, thus indicating the aging of the sea salt aerosol reaching the CARE site.

In between the second and third peak, a decrease in SSCAAE (Fig. 1), SSA (Fig. S4), and concentrations of typical sea salt components together with increases in EC and $\sigma_a(\lambda)$ accounted for a temporary predominance of local urban emissions, as further confirmed by a corresponding decrease in wind speed (not shown).

The assignment of the observed properties to the advection of marine aerosol was also supported by back trajectory analysis (see Fig. S9).

The SSCAAE peak (Fig. 1) registered between February 24th and 25th highlighted the second episode, when low SAE(450,635) (below 0.5) and high AAE(450,635) (above 1.5) were also observed. In addition, a different response by dAAE(450,635,880) and dAAE (450,525,635) was recorded with high and low values, respectively, thus pointing at the smaller absorption spectral curvature at longer wavelengths compared to the shorter ones. In the literature, SAE with values comparable to zero have often been reported as an indication of desert dust detected at the studied site (e.g. Andreae et al., 2002; Yang et al., 2009; Costabile et al., 2013; Ealo et al., 2016; Titos et al., 2017; Lihavainen et al., 2017; Horvath et al., 2018; Romano et al., 2019). Indeed, SAE is linked to particle size (as described in Section 3) and desert aerosol is generally characterised by a large-sized particle contribution greater than in typical urban background PM. Advection

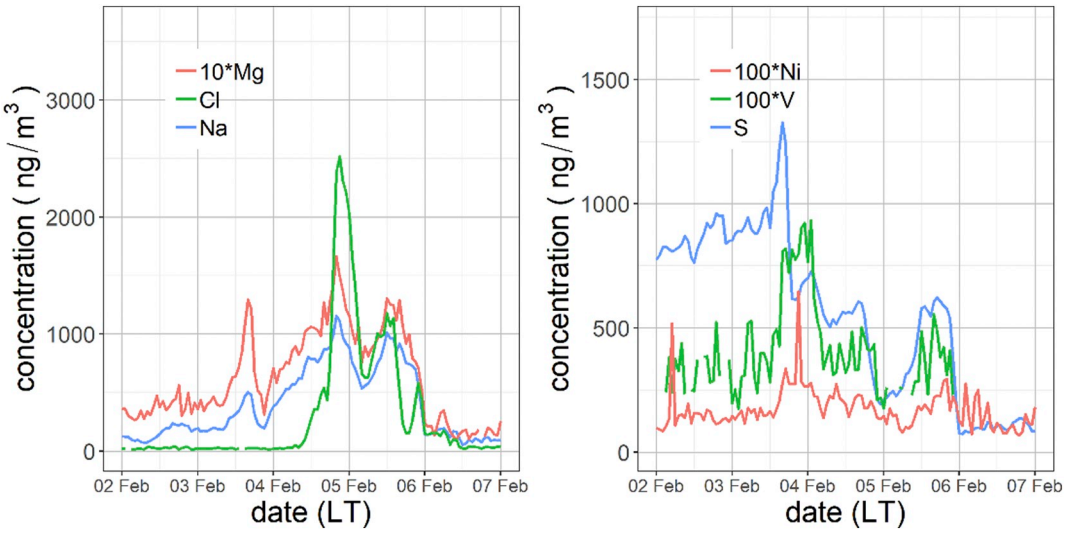

Fig. 2. Concentrations of Na, Mg, Cl, V, Ni, and S in PM2.5 during the CARE campaign.

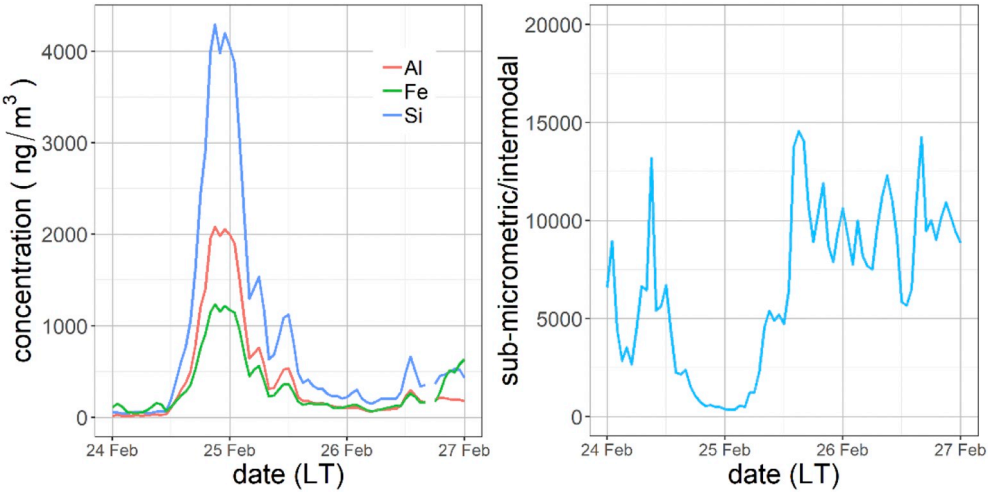

Fig. 3. On the left: concentrations of Al, Si, and Fe in PM2.5. On the right: Ratio of sub-micrometric/intermodal particle number. The period represented refers to the Saharan dust episode.

events of desert aerosol have usually been associated to AAE significantly larger than one (in the range 1.2–3.5 – Collaud Coen et al., 2004; Fialho et al., 2006; Yang et al., 2009; Lee et al., 2012; Costabile et al., 2013; Lihavainen et al., 2017; Romano et al., 2019), in contrast to sea salt aerosol (exhibiting similar SAE but lower AAE). Moreover, it has been shown (e.g. Collaud Coen et al., 2004; Yang et al., 2009) that a non-negligible SSA wavelength dependence and more specifically negative SSAAE values, can be attributed to the predominance of large particles, usually associated with desert dust.

All these considerations, together with the combined temporal patterns of different optical properties (see Figs. 1, S2, S3, S4) were suggestive of an episode of desert dust transported to the CARE sampling site between February 24th and 25th. To confirm the hypothesis of a Saharan dust transport, size-segregated particle number and chemical composition were also investigated. The sub-micrometric/intermodal ratio showed a sharp decrease compared to days close in time and concentration of dust elemental tracers showed a huge increase (Fig. 3) (Nava et al., 2012; Gobbi et al., 2019).

Back-trajectory analysis evidenced that the air mass reaching the CARE site during the night between February 24th and 25th had passed over the Sahara desert at ground level on February 22nd and then reached the sampling site after crossing the Mediterranean at higher altitudes (see Fig. S10).

4.1.2. Local sources dominated aerosol types

Another feature shown by SSCAAE was a narrow peak on February 26th afternoon (Fig. 1), when smoke was seen by researchers working at the CARE site. Indeed, around 13:00 (LT) a large amount of smoke was noticed at Stadium Caracalla and at 18:00 (LT) smoke was smelled at Terme di Caracalla, nearby the CARE sampling site.

As shown in Fig. 1, during this episode AAE(450,635) reached its highest value indicating the presence of relatively small particles (SAE was about 1) with an absorption wavelength dependence stronger than the one of BC. This was likely due to the presence of Brown Carbon (BrC) and it was consistent with the presence of combustion-generated emissions. As reported in Fig. 4, a sharp increase in the biomass burning tracer BBOA was observed during the event (Fig. 4); it is noteworthy that the concomitant occurrence of AAE(450,635) and dAAE (450,635,880) peaks reinforced the attribution to a short fire episode characterised by absorbing particles with a stronger absorption at shortest wavelengths. The Radon temporal pattern (Fig. S11) revealed that the fire episode occurred during well-mixed atmospheric condition (low Radon values) while soon after a strong atmospheric stability affected the monitoring site thus promoting the pollutants accumulation

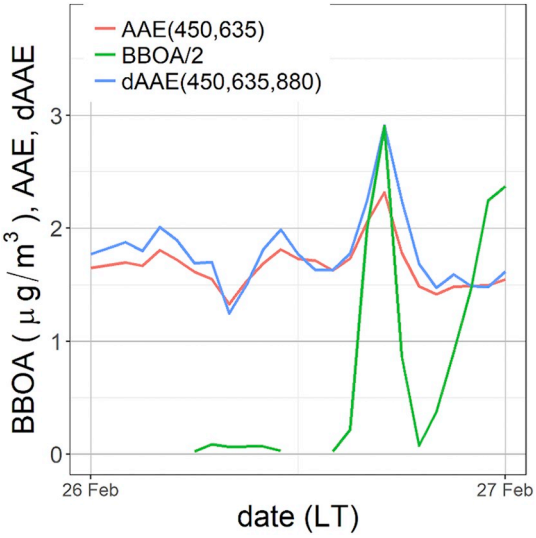

Fig. 4. Temporal patterns of AAE(450,635), dAAE(450,635,880), and BBOA concentration during the biomass burning event of February 26th, 2017.

(high Radon values and BBOA peak).

The central part of the CARE campaign (from February 11th to 22nd) was characterised by atmospheric stability (see Fig. S11), with low wind speeds and clear sky. During this period, high $\sigma_a(635)$ values (> 50 Mm^{-1}) especially in the evening were recorded. Low SSA(635) values (very often below 0.8), SSCAAE(450,635) $<$ 0.65 and mean SAE(450,635) and AAE(450,635) values of 1.33 $\pm$ 0.19 and 1.57 $\pm$ 0.23, respectively, were observed. These aerosol characteristics pointed at a mixture of local emissions from traffic rush hours and biomass burning used for domestic heating. Indeed, the SAE and AAE values indicated a dominance of small particles with quite a strong absorption wavelength dependence, as the one caused by BrC. In the central period of the campaign wind speed was low (average $\pm$ standard deviation: 1.46 $\pm$ 0.89 m/s) suggesting a major role of local aerosol sources.

Multi-wavelength high-time resolved absorption coefficient data were used to perform an optical source apportionment through the well-known Aethalometer model (see Section 3). The two sources considered in the model (fossil fuels - FF and biomass burning - BB) should give the highest contributions at 880 nm and 450 nm (i.e. the longest and the shortest wavelengths used here for aerosol absorption

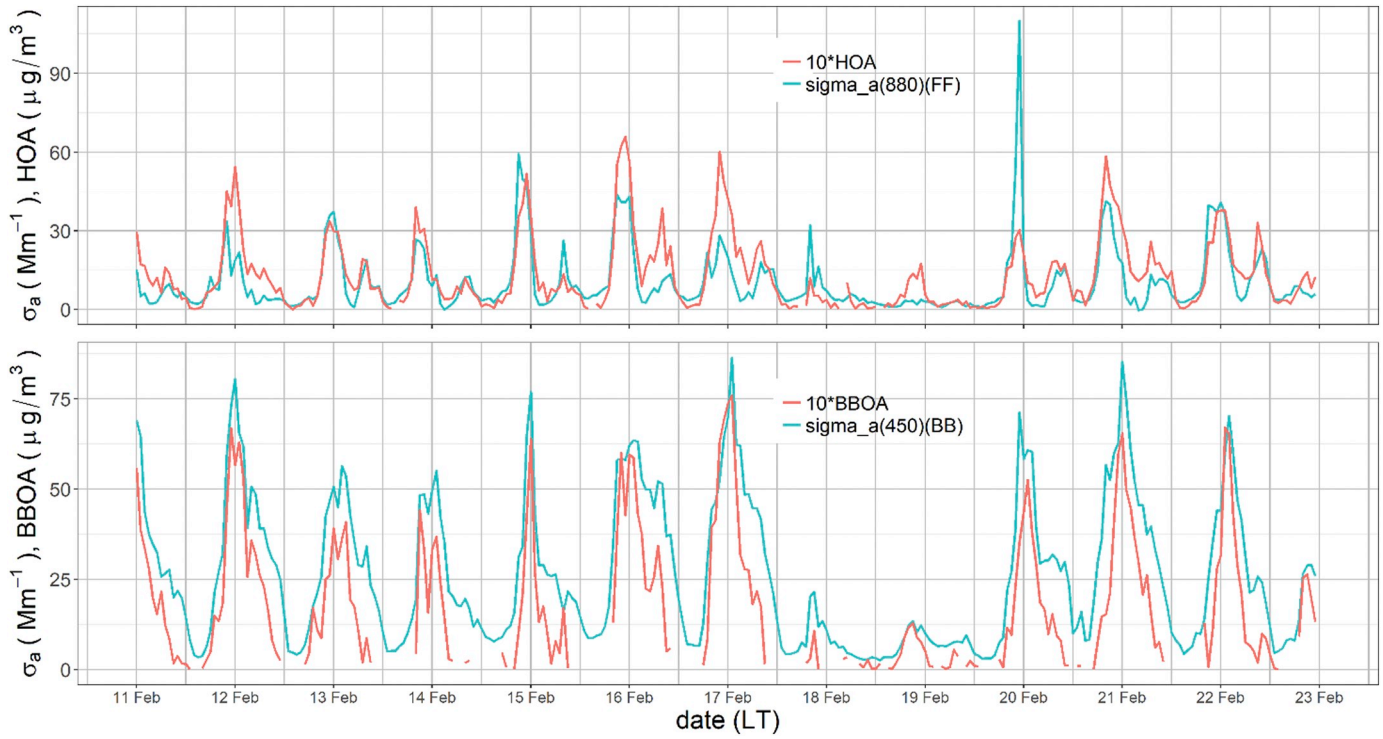

Fig. 5. Top panel: Temporal patterns of σ_a(880)(FF) and HOA concentration. Bottom panel Temporal patterns of σ_a(450)(BB) and BBOA concentration. Absorption coefficients were averaged over 1 h to match OAs time resolution. Only data in the central part of the campaign (February 11–22) are represented.

properties) due to the different absorption spectral dependence of aerosol particles emitted by FF and BB. Therefore, σ_a(880)(FF) and σ_a(450)(BB) were taken as representative parameters for periods dominated by traffic and biomass burning emissions, respectively, as also confirmed by the similarity in temporal patterns of HOA and BBOA (Fig. 5).

Increased concentration of EC and HOA, typically associated to traffic emissions, were detected as well (Figs. S6 and S7).

In Fig. 6 diurnal cycles of number concentration for ultrafine particles (< 0.1 μm in size, UFPs) and for particles in the size range 0.1–1 μm during working days are shown; as expected, UFPs peaked during traffic rush hours, confirming that the dominant contribution during these hours was given by very small particles from fresh vehicular emissions. In addition, particles in the 0.1–1 μm size fraction showed similar peaks but remained higher during the night, probably due to the effect of emissions from domestic heating combined with the daily evolution of the boundary layer height.

4.2. Graphical aerosol classification schemes

Some aerosol classification schemes based on the combination of aerosol properties will be presented in the following with the aim of providing graphical tools that can be useful to quickly distinguish specific events out of a complex dataset comprising optical variables.

Ranges of intensive optical properties allowing to best discriminate among aerosol types identified during the CARE campaign were derived based on the comprehensive analyses previously reported.

In Table 2 ranges of the optical parameters used to classify each type are listed; all the reported conditions should be met in order to robustly identify different aerosol types.

In this work, six main aerosol types were classified. The identification of aerosol particles originated by vehicular traffic and biomass burning during the atmospheric stable period (see Section 4.1.2) was the most difficult task as the intensive optical properties were not sufficient to discriminate the two aerosol types. Therefore, the information retrieved by the Aethalometer model (see Sections 3 and 4.1.2) was

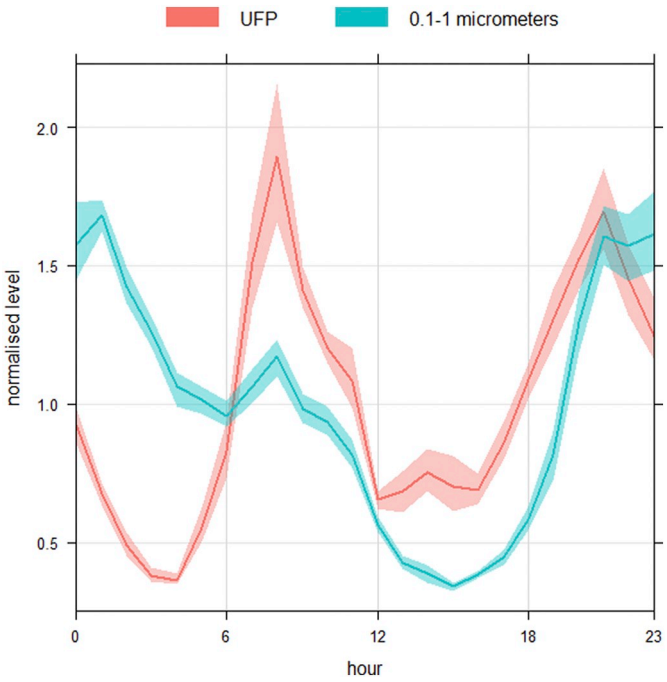

Fig. 6. Diurnal variation (normalised, in local time) of particle number concentration for UFPs and particles in the 0.1–1 μm size fraction. Data refer to the central part of the campaign (February 11–22).

added to identify periods when aerosol was dominated by traffic or biomass burning emissions.

Together, the polluted and the clean marine air masses advected to the sampling site occurred in 7.9% of the cases (i.e. whole CARE dataset); desert dust data covered 2.7% of the cases; data referring to the fire event were 0.3% of the cases; traffic and biomass burning data represented 20.6% and 17.2% of the cases, respectively.

Table 2
Ranges of optical parameters useful to classify aerosol types. σ_a is given in Mm^{-1}. Note that "dust" stands for desert aerosol; "sea" and "polluted marine" stand respectively for the first sub-event and the second and third sub-events of the sea salt aerosol advection episode; "fire" stands for the short biomass burning episode; "traffic" indicates periods dominated by traffic emissions; "BB" indicates periods dominated by the contribution of biomass burning for residential heating.

Aerosol type	SSCAAE (450,635)	SAE (450,635)	AAE (450,635)	dAAE (450,635,880)	dAAE (450,525,635)	SSA (635)	σ_a (450)(BB)	σ_a (880)(FF)
Dust	> 0.6	< 0.4	> 1.5	> 1.6	< 0.2	> 0.8	–	–
Sea	> 0.6	< 0.4	< 1.5	< 1.7	< 0.2	> 0.8	–	–
Polluted marine	0.6–0.9	0.3–0.8	< 1.5	1.0–1.5	−1.0-0.0	> 0.9	–	–
Fire	> 0.8	> 0.7	> 1.8	> 2.0	> 0	–	–	–
Traffic	< 0.2	–	–	–	–	< 0.85	–	> 8
BB	< 0.65	–	–	–	–	–	> 20	–

Table 3
AAE, SAE and SSA values used to classify aerosol types in literature works and this study.

Reference	Columnar/in situ properties	Wavelengths (nm)	Aerosol type	AAE	SAE	SSA
Bahadur et al., 2012	Columnar (AERONET)	440, 675	Dust	> 1.5	< 0.5	–
			Biomass burning	0.5–2	1–2	–
			Urban fossil	< 1.5	0.5–2	–
Cazorla et al., 2013	Columnar (AERONET)	440, 675	Dust	> 1.5	< 1	
			Coated large particles	< 1	< 1.5	–
			OC dominated	> 1.5	> 1.5	–
			EC dominated	< 1	> 1.5	–
Cappa et al., 2016	In-situ	532, 600 (AAE)	Dust	> 2	< 0.2	–
		450, 550 (SAE)	Large particle/low absorption mix	< 1	< 1	–
			Strong BrC	> 2	> 1.5	–
			BC dominated	1.0–1.5	> 1	–
Costabile et al., 2013	In-situ	467, 660 (SSA at 530 nm)	Dust	2	< 0.5	> 0.85
			Marine	> 2	< 0.5	> 0.95
			BC dominated	< 1.5	> 2	< 0.8
			Brown carbon	> 2.5	0.5–2	> 0.9
Schmeisser et al., 2017	In-situ	450, 700	Biomass burning	< 2	1–3	< 0.85
			Dust	> 1.5	< 1	–
			Polluted marine	0.9–1.4	0.7–1.7	–
			Remote marine	0.5–1.5	< 1	–
Romano et al., 2019	In-situ	470, 660	Continental polluted	1–1.5	> 1.4	–
			Dust	> 2	< −0.2	–
			Marine	< 1.2	< 0	–
Rupakheti et al., 2019	Columnar (AERONET)	440–870 (EAE instead of SAE, SSA at 675 nm)	Dust	1.0–3.0	0.0–0.4	0.88–0.96
			Biomass burning	1.1–2.3	0.8–1.7	0.82–0.91
			Urban/Industrial	0.6–1.3	0.8–1.6	0.89–0.96
This study	In-situ	450, 635 (SSA at 635 nm)	Dust	> 1.5	< 0.4	> 0.8
			Sea	< 1.5	< 0.4	> 0.8
			Polluted marine	< 1.5	0.3–0.8	> 0.9
			Fire	> 1.8	> 0.7	–
			Traffic	< 1.7	> 0.7	< 0.85
			BB	> 1.5	> 1.0	–

Table 3 reports ranges of AAE, SAE, and SSA that were used in previous studies to classify aerosol types. Indeed, AAE and SAE were the most commonly employed parameters, usually combined to assess aerosol origin. In some works, information about SSA was added to help the distinction.

Table 3 shows that AAE and SAE values used in this study are generally in agreement with literature values; differences may be due to the wavelengths used in the calculation of intensive optical properties, as well as to the fact that columnar or in-situ properties are employed. It has to be noted that episode-discriminating values reported in Table 2 are in principle wavelength-dependent, thus they are expected to be different if other wavelengths are employed for the calculation of intensive optical properties. Moreover, they may differ depending on the location and season, due to the mixing of pure aerosol types with local emissions, that could affect optical properties. Therefore, in the perspective of using such approach in monitoring networks, it is strongly suggested to perform a preliminary study to check the most suitable ranges of optical variables. Nevertheless, graphical frameworks presented in the following can serve as guides to identify possible episodes simply observing where data are located in each plot.

After identification and selection of the events, data with 5-min resolution were represented in some graphical schemes. In Figs. 7 and 8, the left panel represents data classified as a particular aerosol type according to the methodology described above, whereas the right panel shows the rest of the data (not classified). Data points belonging to different aerosol types are distinguished using different symbols.

4.2.1. AAE vs SAE plot

AAE vs. SAE plot was originally developed in literature for data retrieved from the AERONET network (Russell et al., 2010) and then refined by Cazorla et al. (2013). Other authors (e.g. Cappa et al., 2016; Romano et al., 2019) applied the same methodology to in-situ ground-based data. The graphical classification scheme in Fig. 7 is the AAE vs SAE plot, colour-coded by SSA(635) following Costabile et al. (2013).

As expected from the values reported in the look-up table (Table 2), when representing episodes in a plane, the corresponding data points are placed in different areas. It can be noted that "ship", "sea", "dust" and "fire" data are largely not mixed with non-classified data in the respective plot areas, as emerges also from Fig. 7 (right panel), where some zones of the graph are not covered by points. Points classified as "ship" or "sea" (i.e. marine air masses) are the majority of data in the area defined by (SAE < 0.8 and AAE < 1.5); they were considered together since they are mixed in the graphical scheme. "Traffic" and "BB" points, although not completely overlapped, are also mixed with

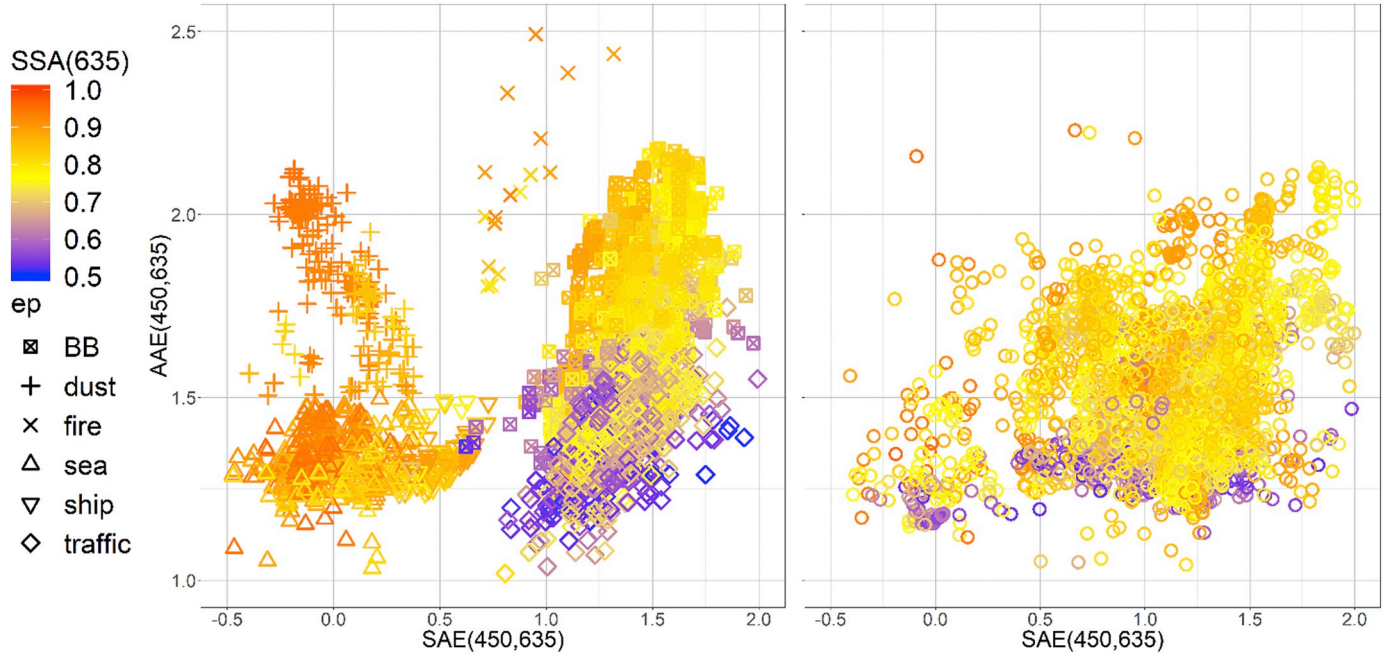

Fig. 7. AAE vs SAE plot colour-coded by SSA(635). On the left: data related to an aerosol type. On the right: all the remaining – i.e. non classified – data. Different symbols represent data of identified aerosol types. BB stands for biomass burning. Note that "ship" stands for the polluted marine event and "fire" for the short biomass burning event.

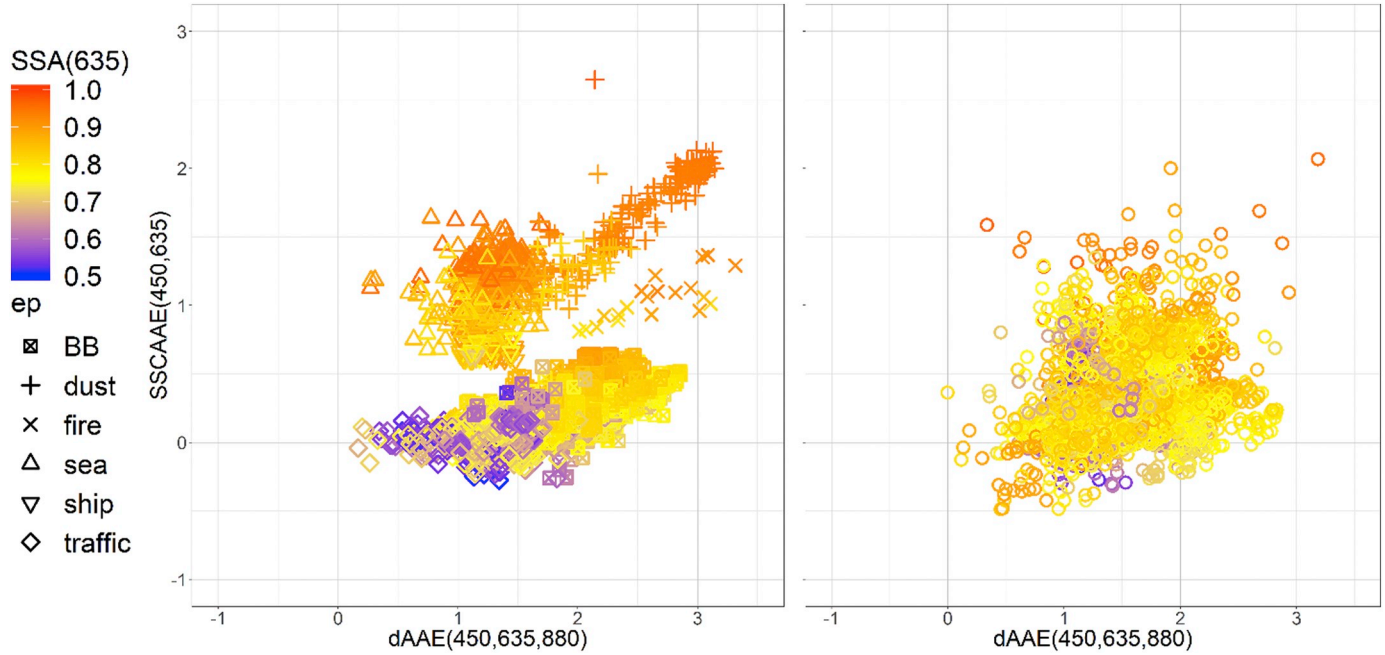

Fig. 8. SSCAAE vs dAAE plot colour-coded by SSA(635). On the left: data related to an aerosol type. On the right: all the remaining – i.e. non classified – data. Different symbols represent data of identified aerosol types. BB stands for biomass burning. Note that "ship" stands for the polluted marine event and "fire" for the short biomass burning event.

each other, reflecting the mixture of local sources contributing to atmospheric aerosol during the central part of the experiment.

The AAE vs SAE plot together with the third coordinate (SSA) helped in the visual discrimination of episodes, even though no ideal SAE, AAE, and SSA ranges were found to correctly classify the first sea salt advection (dominated by ship emissions) without the combined use of SSCAAE and dAAE, that allowed to distinguish this aerosol sub-type.

Therefore, a detailed analysis of temporal patterns of different intensive optical properties (especially SSCAAE) gives a more complete set of information which can be used to distinguish all the events that may have occurred during a campaign. Moreover, for more complex mixtures of aerosol from different sources (when atmospheric stability occurs), the additional information from high-time resolved extensive optical properties is necessary to separate the dominant contribution.

4.2.2. SSCAAE vs dAAE plot

The second graphical framework proposed is a SSCAAE vs dAAE plot (Fig. 8), colour-coded by SSA(635). As far as the authors know, no other study has used a similar scheme to distinguish episodes and aerosol types.

This new scheme (Fig. 8) confirmed the potential of SSCAAE as a key parameter for episodes identification. Indeed, except for urban aerosol, all the other aerosol types were characterised by SSCAAE (450,635) > 0.5. The combination with dAAE(450,635,880) helped to discriminate events, since this parameter responds to non-uniform absorption spectral dependence that can be different for episodes with similar SSCAAE values. For instance, this was the case of "sea" and "fire" aerosol types, characterised respectively by mean SSCAAE (450,635) equal to 1.16 ± 0.18 and 1.05 ± 0.17 and mean dAAE (450,635,880) of 1.25 ± 0.21 and 2.65 ± 0.39, respectively.

Also in this case episodes are placed in different regions of the plane and some areas are not well covered by data points when considering only non-classified data (Fig. 8 – right). In this graphical framework some aerosol types (in particular "dust", and to a less extent "fire") show an almost linear relationship between SSCAAE and dAAE. Finally, local-sources dominated periods are characterised by an almost λ-independent co-albedo (SSCAAE ≈ 0) and by an increase in the absorption spectral curvature as the contribution of biomass burning emissions increases compared to the one from vehicular traffic.

The SSCAAE vs dAAE plot and AAE vs SAE plot are useful to provide a first hint about episodes and aerosol typologies. Nevertheless, 2D plots areas do not correspond uniquely to different aerosol types; especially aerosol mixtures impacted by local sources are not distinguishable from not classified data, since zones where the two populations are located in the plots overlap. This is a limitation of 2D plots when plotting all data (both classified and unclassified) together as urban aerosol mixtures produce a cloud of points comprehending both traffic- and biomass burning-related emissions. In complex situations, it is the separate study of temporal patterns of all the intensive optical parameters (SSCAAE, SAE, AAE, and dAAE) that can provide further information to distinguish aerosol with different origins.

5. Conclusions

Aerosol physical-chemical and optical properties measured at high time resolution during the CARE experiment were analysed to classify different aerosol types, both from advection episodes and by local source emissions.

In particular, this study was focused on multi-wavelength optical properties measured by widespread on-line instrumentation (i.e. Nephelometer, Aethalometer, and MAAP). It has to be noted that, when analysing such kind of data, attention has to be paid to their interpretation and elaboration, since they require non-negligible corrections to take into account biases due to the filter matrix (e.g. for the Aethalometer) and for truncation effects (for the Nephelometer).

In this work, scattering and absorption coefficients were employed to obtain several intensive optical parameters. At the CARE monitoring site, the wavelength dependence of the co-albedo (SSCAAE) was the most effective parameter in discriminating between aerosol particles dominated by air masses advection or influenced by local emissions; SSCAAE can be, therefore, a good candidate to be tested in similar studies in the future. Nevertheless, even exploiting the high time resolution, only a combination of several optical properties led to a better classification of different aerosol types. Chemical composition and size distribution data were employed to confirm the advection episodes and aerosol types identified by the optical parameters. Due to difficulties in disentangling local source emissions impacting on aerosol properties in atmospheric stagnant conditions, the well-known Aethalometer model was applied which helped in identifying the contribution of traffic and biomass burning to the absorption coefficient measured at different wavelengths.

Graphical classification schemes developed in this work represented useful tools to get a first classification of aerosol particles based on optical intensive parameters for specific aerosol advection events. At the same time, this work clearly showed that a more robust aerosol classification can be obtained by observing temporal patterns of optical parameters. Although based on the analysis of few episodes, the complete aerosol chemical speciation and the availability of number size distributions confirmed the nature of the episodes detected by optical parameters.

The methodology here applied can be replicated at any site to generate specific look-up tables or using the one reported in this work at sites with similar characteristics; this approach can be useful to discriminate in near-real-time between pollution vs. natural sources-driven high PM events in environmental monitoring networks using optical parameters only. Of course, this procedure is much simpler than e.g. the methodology officially accepted by the European Commission (see e.g. Querol et al., 2019) to estimate the African dust outbreaks but provides hints also on the impact from other aerosol sources.

Author contributions

SV drafted the paper and performed the data analysis; RV proposed the topic of this paper and contributed to the the synthesis of the results; VB, ACF, and GV collaborated to data analysis and interpretation; FB, FC, LDL, and GPG took care of the whole campaign, performed optical data measurements, data reduction and contributed to data interpretation; GC, FL, and SN carried out streaker sampling, PIXE analysis, EC/OC measurements and data analysis; MG and EP provided ACSM data and performed PMF analysis to retrieve BBOA, HOA, and OOA data; AW provided MAAP data. All authors contributed to the interpretation of the results obtained with the approach here described and revised the manuscript content giving a final approval of the version to be submitted. RV and SV reviewed the paper addressing reviewers' comments.

Data availability

The data in the study are available from the authors upon request (roberta.vecchi@unimi.it).

Declaration of Competing Interest

The authors declare no conflict of interest.

Appendix A. Supplementary data

Supplementary data to this article can be found online at https://doi.org/10.1016/j.atmosres.2019.104799.

References

IPCC, Climate Change, 2013. The Physical Science Basis. Working Group I Contribution to the Fifth Assessment Report of the Intergovernmental Panel on Climate Change - IPCC. http://www.ipcc.ch/report/ar5/wg1/.

Alas, H.D.C., Weinhold, K., Costabile, F., Di Ianni, A., Müller, T., Pfeifer, S., Di Liberto, L., Turner, J.R., Wiedensohler, A., 2019. Methodology for High Quality Mobile Measurement with Focus on Black Carbon and Particle Mass Concentrations. Atmos. Meas. Tech. 12, 4697–4712. https://doi.org/10.5194/amt-12-4697-2019.

Andreae, T.W., Andreae, M.O., Ichoku, C., Maenhaut, W., Cafmeier, J., Kamieli, A., Orlowski, L., 2002. Light scattering by dust and anthropogenic aerosol at a remote site in the Negev desert. Israel. J. Geophys. Res. 107 (D2), 4008. https://doi.org/10.1029/2001JD900252.

Bahadur, R., Praveen, P.S., Xu, Y., Ramanathan, V., 2012. Solar absorption by elemental and brown carbon determined from spectral observations. PNAS 109, 43.

Barnaba, F., Gobbi, G.P., 2004. Aerosol seasonal variability over the Mediterranean region and relative impact of maritime, continental and Saharan dust particles over the basin from MODIS data in the year 2001. Atmos. Chem. Phys. 4, 2367–2391.

Barnaba, F., Bolignano, A., Di Liberto, L., Morelli, M., Lucarelli, F., Nava, S., Perrino, C., Canepari, S., Basart, S., Costabile, F., Dionisi, D., Ciampichetti, S., Sozzi, R., Gobbi, G.P., 2017. Desert dust contribution to PM10 loads in Italy: Methods and recommendations addressing the relevant European Commission guidelines in support to the Air Quality Directive 2008/50. Atmos. Environ. 161, 288–305. https://doi.org/10.1016/j.atmosenv.2017.04.038.

Bond, T.C., Bergstrom, R.V., 2006. Light Absorption by Carbonaceous Particles: an Investigative Review. Aerosol Sci. Technol. 40, 27–67. https://doi.org/10.1080/02786820500421521.

Calzolai, G., Lucarelli, F., Chiari, M., Nava, S., Giannoni, M., Carraresi, L., Prati, P., Vecchi, R., 2015. Improvements in PIXE analysis of hourly particulate matter samples. Nucl. Instr. Meth. B 363, 99–104. https://doi.org/10.1016/j.nimb.2015.08.022.

Canonaco, F., Crippa, M., Slowik, J.G., Baltensperger, U., Prévôt, A.S.H., 2013. SoFi, an IGOR-based interface for the efficient use of the generalized multilinear engine (ME-2) for the source apportionment: ME-2 application to aerosol mass spectrometer data. Atmos. Meas. Tech. 6, 3649–3661. https://doi.org/10.5194/amt-6-3649-2013.

Cappa, C.D., Kolesar, K.R., Zhang, X., Atkinson, D.B., Pekour, M.S., Zaveri, R.A., Zelenyuk, A., Zhang, Q., 2016. Understanding the optical properties of ambient sub- and supermicron particulate matter: results from the CARES 2010 field study in northern California. Atmos. Chem. Phys. 16, 6511–6535. https://doi.org/10.5194/acp-16-6511-2016.

Cazorla, A., Bahadur, R., Suski, K.J., Cahill, J.F., Chand, D., Schmid, B., Ramanathan, V., Prather, K.A., 2013. Relating aerosol absorption due to soot, organic carbon, and dust to emission sources determined from in-situ chemical measurements. Atmos. Chem. Phys. 13, 9337–9350. https://doi.org/10.5194/acp-13-9337-2013.

Collaud Coen, M., Weingartner, E., Schaub, D., Hueglin, C., Corrigan, C., Henning, S., Schwikowski, M., Baltensperger, U., 2004. Saharan dust events at the Jungfraujoch: detection by wavelength dependence of the single scattering albedo and first climatology analysis. Atmos. Chem. Phys. 4, 2465–2480. www.atmos-chem-phys.org/acp/4/2465/.

Collaud Coen, M., Weingartner, E., Apituley, A., Ceburnis, D., Fierz-Schmidhauser, R., Flentje, H., Henzing, J.S., Jennings, S.G., Moerman, M., Petzold, A., Schmid, O., Baltensperger, U., 2010. Minimizing light absorption measurement artifacts of the Aethalometer: evaluation of five correction algorithms. Atmos. Meas. Tech. 3, 457–474. www.atmos-meas-tech.net/3/457/2010/.

Costabile, F., Barnaba, F., Angelini, F., Gobbi, G.P., 2013. Identification of key aerosol populations through their size and composition resolved spectral scattering and absorption. Atmos. Chem. Phys. 13, 2455–2470. https://doi.org/10.5194/acp-13-2455-2013.

Costabile, F., Alas, H., Aufderheide, M., Avino, P., Amato, F., Argentini, S., Barnaba, F., Berico, M., Bernardoni, V., Biondi, R., Calzolai, G., Canepari, S., Casasanta, G., Ciampichetti, S., Conidi, A., Cordelli, E., Di Ianni, A., Di Liberto, L., Facchini, M.C., Facci, A., Frasca, D., Gilardnoni, S., Grollino, M.G., Gualtieri, M., Lucarelli, F., Malaguti, A., Manigrasso, M., Montagnoli, M., Nava, S., Padoan, E., Perrino, C., Petralia, E., Petenko, I., Querol, X., Simonetti, G., Tranfo, G., Ubertini, S., Valli, G., Valentini, S., Vecchi, R., Volpi, F., Weinhold, K., Wiedensholer, A., Zanini, G., Gobbi, G.P., 2017. First results of the "Carbonaceous Aerosol in Rome and Environs (CARE)" Experiment: beyond Current Standards for PM_{10}. Atmosphere 8, 249. https://doi.org/10.3390/atmos8120249.

Costabile, F., Gualtieri, M., Canepari, S., Tranfo, G., Consales, C., Grollino, M.G., Paci, E., Petralia, E., Pigini, D., Simonetti, G., 2019. Evidence of association between aerosol properties and in-vitro cellular oxidative response to PM1, oxidative potential of PM2.5, a biomarker of RNA oxidation, and its dependency on the combustion aerosol. Atmos. Environ. 213, 445–455. https://doi.org/10.1016/j.atmosenv.2019.06.023.

Diapouli, E., Manousakas, M.I., Vratolis, S., Vasilatou, V., Pateraki, S., Bairachtari, K.A., Querol, X., Amato, F., Alastuey, A., Karanasiou, A.A., Lucarelli, F., Nava, S., Calzolai, G., Gianelle, V.L., Colombi, C., Alves, C., Custódio, D., Pio, C., Spyrou, C., Kallos, G.B., Eleftheriadis, K., 2017. AIRUSE-LIFE+: estimation of natural source contributions to urban ambient air PM10 and PM2:5 concentrations in southern Europe – implications to compliance with limit values. Atmos. Chem. Phys. 17, 3673–3685. https://doi.org/10.5194/acp-17-3673-2017.

Dockery, D.W., Pope, C.A., Xu, X., Spengler, J.D., Ware, J.H., Fay, M.E., Ferris, B.G., Speizer, F.E., 1993. An Association between Air Pollution and Mortality in six U.S. Cities. N. Engl. J. Med. 329, 1753–1759.

Donateo, A., Lo Feudo, T., Marinoni, A., Dinoi, A., Avolio, E., Merico, E., Calidonna, C.R., Contini, D., Bonasoni, P., 2018. Characterization of in Situ Aerosol Optical Properties at three Observatories in the Central Mediterranean. Atmosphere 9, 369. https://doi.org/10.3390/atmos9100369.

Drinovec, L., Močnik, G., Zotter, P., Prévôt, A.S.H., Ruckstuhl, C., Coz, E., Rupakheti, M., Sciare, J., Müller, T., Wiedensohler, E., Hansen, D.A., 2015. The "dual-spot" Aethalometer: an improved measurement of aerosol black carbon with real-time loading compensation. Atmos. Measur. Tech. 8, 1965–1979. https://doi.org/10.5194/amt-8-1965-2015.

Dubovik, O., Holben, B., Eck, T.F., Smirnov, A., Kaufman, Y.J., King, M.D., Tanré, D., Slutsker, I., 2002. Variability of Absorption and Optical Properties of Key Aerosol Types Observed in Worldwide Locations. J. Atmos. Sci. 59, 590–608.

Ealo, M., Alastuey, A., Ripoll, A., Pérez, N., Minguillón, M.C., Querol, X., Pandolfi, M., 2016. Detection of Saharan dust and biomass burning events using near-real-time intensive aerosol optical properties in the North-Western Mediterranean. Atmos. Chem. Phys. 16, 12567–12586. https://doi.org/10.5194/acp-16-12567-2016.

Eck, T.F., Holben, B.N., Reis, J.S., Dubovik, O., Smirnov, A., O'Neill, N.T., Slutsker, I., Kinne, S., 1999. Wavelength dependence of the optical depth of biomass burning, urban, and desert dust aerosols. J. Geophys. Res. 104 (D24), 31333–31349.

Fialho, P., Freitas, M.C., Barata, F., Vieira, B., Hansen, A.D.A., Honrath, R.E., 2006. The Aethalometer calibration and determination of iron concentration in dust aerosols. J. Aerosol Sci. 37, 1497–1506. https://doi.org/10.1016/j.jaerosci.2006.03.002.

Giles, D.M., Holben, B.N., Tripathi, S.N., Eck, T.F., Newcomb, W.N., Slutsker, I., Dickerson, R.R., Thompson, A.M., Mattoo, S., Wang, S.-H., Singh, R.P., Sinyuk, A., Schafer, J.S., 2011. Aerosol properties over the Indo-Gangetic Plain: a mesoscale perspective from the TIGERZ experiment. J. Geophys. Res. 116https://doi.org/10.1029/2011JD015809. D18203.

Giles, D.M., Holben, B.N., Eck, T.F., Sinyuk, A., Smirnov, A., Slutsker, I., Dickerson, R.R., Thompson, A.M., Schafer, J.S., 2012. An analysis of AERONET aerosol absorption properties and classifications representative of aerosol source regions. J. Geophys. Res. 117https://doi.org/10.1029/2012JD018127. D17203.

Gobbi, G.P., Kaufman, Y.J., Koren, I., Eck, T.F., 2007. Classification of aerosol properties derived from AERONET direct sun data. Atmos. Chem. Phys. 7, 453–458. www.atmos-chem-phys.net/7/453/2007/.

Gobbi, G.P., Barnaba, F., Di Liberto, L., Bolignano, A., Lucarelli, F., Nava, S., Perrino, C., Pietrodangelo, A., Basart, S., Costabile, F., Dionisi, D., Rizza, U., Canepari, S., Sozzi, R., Morelli, M., Manigrasso, M., Drenwick, F., Stuckmeier, C., Poenitz, K., Wille, K., 2019. An inclusive view of Saharan dust advections to Italy and the Central Mediterranean. Atmos. Environ. 2019, 242–256. https://doi.org/10.1016/j.atmosenv.2019.01.002.

Goetz, J.D., Giordano, M.R., Stockwell, C.E., Christian, T.J., Maharian, R., Adhikari, S., Bhave, P.V., Praveen, P.S., Panday, A.K., Jayarathne, T., Stone, E.A., Yokelson, R.J., DeCarlo, P.F., 2018. Speciated online PM1 from south Asian combustion sources – Part1: Fuel-based emission factors and size distributions. Atmos. Chem. Phys. 18, 14653–14679. https://doi.org/10.5194/acp-18-14653-2018.

Horvath, H., Alados Alarboledas, A., Olmo Reyes, F.J., 2018. Angular scattering of the sahara dust aerosol. Atmos. Chem. Phys. 18, 17735–17744. https://doi.org/10.5194/acp-18-17735-2018.

Hyvärinen, A.P., Vakkari, V., Hooda, R.K., Sharma, V.P., Panwar, T.S., Beukes, J.P., van Zyl, P.G., Josipovic, M., Garland, R.M., Andreae, M.O., Pöschl, U., Petzold, A., 2013. Correction for a measurement artifact of the Multi-Angle Absorption Photometer (MAAP) at high black carbon mass concentration levels. Atmos. Measur. Tech. 6, 81–90. https://doi.org/10.5194/amt-6-81-2013.

Kalapureddy, M.C.R., Kaskaoutis, D.G., Raj, P.E., Devara, P.C.S., Kambezidis, H.D., Kosmopoulos, P.G., Nastos, P.T., 2009. Identification of aerosol type over the Arabian Sea in the premonsoon season during the Integrated Campaign for Aerosol, gases and Radiation Budget (ICARB). J. Geophys. Res. 114, D17203. https://doi.org/10.1029/2009JD011826.

Kaufman, Y.J., 1993. Aerosol optical thickness and atmospheric path radiance. J. Geophys. Res. 98 (D2), 2677–2692.

Khlystov, A., Stanier, C., Pandis, S.N., 2004. An algorithm for combining electrical mobility and aerodynamic size distributions data when measuring ambient aerosol special issue of aerosol science and technology on findings from the fine particulate matter supersites program. Aerosol Sci. Technol. 38, 229–238. https://doi.org/10.1080/02786820390229543.

Lee, S., Yoo, S.-C., Lim, S.-W., Kim, Y.P., Ghim, Y.S., Kim, J.-H., Kang, C.-H., Kim, Y.J., Chang, L.-S., Lee, S.-J., 2012. Spectral dependency of light scattering/absorption and hygroscopicity of pollution and dust aerosols in Northeast Asia. Atmos. Environ. 50, 246–254. https://doi.org/10.1016/j.atmosenv.2011.12.026.

Lihavainen, H., Alghamdi, M.A., Hyvärinen, A., Hussein, T., Neitola, K., Khoder, M., Abdelmaksoud, A.S., Al-Jeelani, H., Shabbaj, I.I., Almehmadi, F.M., 2017. Aerosol optical properties at rural background area in Western Saudi Arabia. Atmos. Res. 197, 370–378. https://doi.org/10.1016/j.atmosres.2017.07.019.

Lucarelli, F., Chiari, M., Calzolai, G., Giannoni, M., Nava, S., Udisti, R., Severi, M., Querol, X., Amato, F., Alves, C., Eleftheriasdis, K., 2015. The role of PIXE in the AIRUSE project "testing and development of air quality mitigation measures in Southern Europe". Nucl. Inst. Methods Phys. Res. B 363, 92–98. https://doi.org/10.1016/j.nimb.2015.08.023.

Moosmüller, H., Chackabarty, R.K., 2011. Technical note: simple analytical relationships between ångström coefficients of aerosol extinction, scattering, absorption, and single scattering albedo. Atmos. Chem. Phys. 11, 10677–10680. https://doi.org/10.5194/acp-11-10677-2011.

Müller, T., Laborde, M., Kassell, G., Wiedensohler, A., 2011a. Design and performance of a three-wavelength LED-based total scatter and backscatter integrating nephelometer. Atmos. Measur. Tech. 4, 1291–1303. https://doi.org/10.5194/amt-4-1291-2011.

Müller, T., Henzing, J.S., de Leeuw, G., Wiedensohler, E., Alastuey, A., Angelov, H., Bizjak, M., Collaud, Coen M., Engström, J.E., Gruening, C., Hillamo, R., Hoffer, A., Imre, K., Ivanow, P., Jennings, G., Sun, J.Y., Kalivitis, N., Karlsson, H., Komppula, M., Laj, P., Li, S.-M., Lunder, C., Marinoni, A., Martins dos Santos, S., Moerman, M., Nowak, A., Ogren, J.A., Petzold, A., Pichon, J.M., Rodriquez, S., Sharma, S., Sheridan, P.J., Teinilä, K., Tuch, T., Viana, M., Weingartner, E., Wilhelm, R., Wang, Y.Q., 2011b. Characterization and intercomparison of aerosol absorption photometers: results of two intercomparison workshops. Atmos. Measur. Tech. 4, 245–268. https://doi.org/10.5194/amt-4-245-2011.

Nava, S., Becagli, S., Calzolai, G., Chiari, M., Lucarelli, F., Prati, P., Traversi, R., Udisti, R., Valli, G., Vecchi, R., 2012. Saharan dust impact in Central Italy: an overview on three years elemental data records. Atmos. Environ. 60, 444–452. https://doi.org/10.1016/j.atmosenv.2012.06.064.

Ng, N.L., Herndon, S.C., Trimborn, A., Canagaratna, M.R., Croteau, P., Onasch, T.M., Sueper, D., Worsnop, D.R., Zhang, Q., Sun, Y.L., Jayne, J.T., 2011. An Aerosol Chemical Speciation Monitor (ACSM) for routine monitoring of atmospheric aerosol composition. Aerosol Sci. Technol. 45, 770–784. https://doi.org/10.1080/02786826.2011.560211.

Perrino, C., Canepari, S., Catrambone, M., Dalla Torre, S., Rantica, E., Sargolini, T., 2009. Influence of natural events on the concentration and composition of atmospheric particulate matter. Atmos. Environ. 43, 4766–4779. https://doi.org/10.1016/j.atmosenv.2008.06.035.

Pope, I.I.I.C.A., Burnett, R.T., Thun, M.J., Calle, E.E., Krewski, D., Ito, K., Thurston, G.D., 2002. Lung Cancer, Cardiopulmonary Mortality, and long-term Exposure to Fine Particulate Air Pollution. J. Am. Med. Assoc. 287, 1132–1141.

Querol, X., Pérez, N., Reche, C., Ealo, M., Ripoll, A., Tur, J., Pandolfi, M., Pey, J., Salvador, P., Moreno, T., Alastuey, A., 2019. African dust and air quality over Spain: Is it only dust that matters? Science of the Total Environment 686, 737–752. https://doi.org/10.1016/j.scitotenv.2019.05.349. Ramachandran S, 2018. Atmospheric Aerosols – Characteristics and Radiative Effects. Taylor and Francis; ISBN 1498750737.

Romano, S., Perrone, M.R., Pavese, G., Esposito, F., Calvello, M., 2019. Optical properties of PM2.5 particles: results from a monitoring campaign in southeastern Italy. Atmos. Environ. 203, 35–47. https://doi.org/10.1016/j.atmosenv.2019.01.037.

Rupakheti, D., Kang, S., Bilal, M., Gong, J., Xia, X., Cong, Z., 2019. Aerosol optical depth climatology over Central Asian countries based on Aqua-MODIS Collection 6.1 data: Aerosol variations and sources. Atmos. Environ. 207, 205–214. https://doi.org/10.1016/j.atmosenv.2019.03.020.

Russell, P.B., Bergstrom, R.W., Shinozuka, Y., Clarke, A.D., DeCarlo, P.F., Jimenez, J.L., Livingston, J.M., Redemann, J., Dubovik, O., Strawa, A., 2010. Absorption Angstrom Exponent in AERONET and related data as an indicator of aerosol composition. Atmos. Chem. Phys. 10, 1155–1169. www.atmos-chem-phys.net/10/1155/2010/.

Sandradewi, J., Prévôt, A.S.H., Szidat, S., Perron, N., Alfarra, M.R., Lanz, V.A., Weingartner, E., Baltensperger, U., 2008. Using Aerosol Light Absorption Measurements for the Quantitative Determination of Wood burning and Traffic Emission Contributions to Particulate Matter. Environ. Sci. Technol. 42, 3316–3323.

Schmeisser, L., Andrews, E., Ogren, J.A., Sheridan, P., Jefferson, A., Sharma, S., Kim, J.E., Sherman, J.P., Sorribas, M., Kalapov, I., Arsov, T., Angelov, C., Mayol-Bracero, O.M., Labuschagne, C., Kim, S.-W., Hoffer, A., Lin, N.-H., Chia, H.-P., Bergin, M., Sun, J., Liu, P., Wu, H., 2017. Classifying aerosol type using in situ surface spectral aerosol optical properties. Atmos. Chem. Phys. 17, 12097–12120. https://doi.org/10.5194/acp-17-12097-2017.

Schuster, G.L., Dubovik, O., Holben, B.N., 2006. Angstrom exponent and bimodal aerosol size distributions. J. Geophys. Res. 111, D07207. https://doi.org/10.1029/2005JD006328.

Segura, S., Estellés, V., Titos, G., Lyamani, H., Utrillas, M.P., Zotter, P., Prévôt, A.S.H., Močnik, G., Alados-Alarboledas, L., Martínez-Lozano, J.A., 2014. Determination and analysis of in situ spectral aerosol optical properties by a multi-instrumental approach. Atmos. Measur. Tech. 7, 2373–2387. https://doi.org/10.5194/amt-7-2373-2014.

Seinfeld, J.H., Pandis, S., 1998. Atmospheric Chemistry and Physics. From Air Pollution to Climate Change. Wiley-Interscience.

Takemura, T., Nakajima, T., Dubovik, O., Holben, B.N., Kinne, S., 2002. Single-Scattering Albedo and Radiative Forcing of various Aerosol Species with a Global Three-Dimensional Model. J. Clim. 15 (4).

Timonen, H., Aurela, M., Carbone, S., Saarnio, K., Saarikoski, S., Mäkelä, T., Kulmala, M., Kerminen, V.-M., Worsnop, D.R., Hillamo, R., 2010. High time-resolution chemical characterization of the water-soluble fraction of ambient aerosols with PILS-TOC-IC and AMS. Atmos. Measur. Tech. 3, 1063–1074. https://doi.org/10.5194/amt-3-1063-2010.

Titos, G., Ealo, M., Pandolfi, M., Pérez, N., Sola, Y., Sicard, M., Comerón, A., Querol, X., Alastuey, A., 2017. Spatiotemporal evolution of a severe winter dust event in the western Mediterranean: Aerosol optical and physical properties. J. Geophys. Res. Atmos. 122, 4052–4069. https://doi.org/10.1002/2016JD026252.

Valenzuela, A., Olmo, F.J., Lyamani, H., Antón, M., Titos, G., Cazorla, A., Alados-Alarboledas, L., 2015. Aerosol scattering and absorption Angström exponents as indicators of dust and dust-free days over Granada (Spain). Atmos. Res. 154, 1–13. https://doi.org/10.1016/j.atmosres.2014.10.015.

Viana, M., Amato, F., Alastuey, A., Querol, X., Moreno, T., García Dos Santos, S., Herce, M.D., Fernández-Patier, R., 2009. Chemical Tracers of Particulate Emissions from Commercial Shipping. Environ. Sci. Technol. 43, 7472–7477. https://doi.org/10.1021/es901558t.

Yang, M., Howell, S.G., Zhuang, J., Huebert, B.J., 2009. Attribution of aerosol light absorption to black carbon, brown carbon, and dust in China – interpretations of atmospheric measurements during EAST-AIRE. Atmos. Chem. Phys. 9, 2035–2050. www.atmos-chem-phys.net/9/2035/2009/.

Zotter, P., Herich, H., Gysel, M., El-Haddad, I., Zhang, Y., Močnik, G., Hüglin, C., Baltensperger, U., Szidat, S., Prévôt, A.S.H., 2017. Evaluation of the absorption Ångström exponents for traffic and wood burning in the Aethalometer-based source apportionment using radiocarbon measurements of ambient aerosol. Atmos. Chem. Phys. 17, 4229–4249. Re. https://doi.org/10.5194/acp-17-4229-2017.